

Article

Prominent COF, g-C₃N₄, and Their Heterojunction Materials for Selective Photocatalytic CO₂ Reduction

Panagiota Bika , Ilias Papailias , Tatiana Giannakopoulou , Christos Tampaxis , Theodore A. Steriotis ,
Christos Trapalis and Panagiotis Dallas * 

Institute of Nanoscience and Nanotechnology, National Centre For Scientific Research Demokritos, 15341 Athens, Greece; p.bika@inn.demokritos.gr (P.B.); i.papailias@inn.demokritos.gr (I.P.); t.giannakopoulou@inn.demokritos.gr (T.G.); c.tampaxis@inn.demokritos.gr (C.T.); t.steriotis@inn.demokritos.gr (T.A.S.); c.trapalis@inn.demokritos.gr (C.T.)

* Correspondence: p.dallas@inn.demokritos.gr; Tel.: +30-210-650-3311

Abstract: New heterojunction materials (HJs) were synthesized in-situ by molecularly bonding the monomers of a triazine-based covalent organic framework (bulk COF) on the template of exfoliated carbon nitride (g-C₃N₄). The photocatalysts reduced carbon dioxide to carbon monoxide in aqueous dispersions under UV irradiation. The g-C₃N₄ showed production of 6.50 μmol CO g⁻¹ h⁻¹ and the bulk COF of 2.77 μmol CO g⁻¹ h⁻¹. The CO yield was evaluated in sustainability photoreduction cycles and their CO₂ uptake capacity and isosteric heat of adsorption were estimated. All the heterojunction photocatalysts obtained ameliorated CO production rates compared to the bulk COF. Finally, the influence of the Pt co-catalyst on the photocatalytic activities was determined without the addition of any sacrificial agent, and the COF:g-C₃N₄ heterojunction with the ratio of 1:10 was proven to be a photocatalytic system with an optimum and selective, CO yield of 7.56 μmol g⁻¹ h⁻¹.

Keywords: COF; g-C₃N₄; heterojunction; UV irradiation; CO₂ photoreduction



Citation: Bika, P.; Papailias, I.; Giannakopoulou, T.; Tampaxis, C.; Steriotis, T.A.; Trapalis, C.; Dallas, P. Prominent COF, g-C₃N₄, and Their Heterojunction Materials for Selective Photocatalytic CO₂ Reduction. *Catalysts* **2023**, *13*, 1331. <https://doi.org/10.3390/catal13101331>

Academic Editors: Huazhen Shen, Kangle Lv, Chung-Hsuang Hung and Chung-Shin Yuan

Received: 23 August 2023

Revised: 13 September 2023

Accepted: 27 September 2023

Published: 29 September 2023



Copyright: © 2023 by the authors. Licensee MDPI, Basel, Switzerland. This article is an open access article distributed under the terms and conditions of the Creative Commons Attribution (CC BY) license (<https://creativecommons.org/licenses/by/4.0/>).

1. Introduction

New and effective techniques are being established for the conversion of carbon dioxide to useful, valuable chemicals and fuels by the efficient utilization of abundant solar energy. Until now, inorganic materials such as metals, transition-metal oxides, and chalcogenides with strong absorption coefficients in the ultraviolet and visible spectrum have been employed as photocatalysts for CO₂ reduction, despite their hazardous impact on the environment [1,2].

Accordingly, the synthesis of new organic materials is thriving, replacing inorganic ones [3,4] which contain potentially toxic heavy metal elements [5,6] and metal-organic frameworks [7–10] with metal-free organic layered structures. From graphene and carbon nitride [11,12] to covalent organic frameworks [13,14], these conjugated semiconductors are promising candidates for photocatalytic applications, as their active sites, their porosity, and their modulated, favorable band gap, provide green pathways to the degradation of organic pollutants [15,16], hydrogen production [17] and carbon dioxide photoreduction.

The high dissociation energy of the carbon-oxygen bond renders CO₂ a stable molecule. Concerning the above for the reduction of CO₂, the addition of co-catalysts such as metal complexes, nanoparticles, sacrificial agents, and photosensitizers is considered necessary for an appreciable reaction yield [18–20]. Moreover, the photocatalytic CO₂ reduction to CO may take place in parallel to the competitive evolution of hydrogen [19–21] or unwanted hydrocarbons [18,22,23] either in the gas (CH₄) or the liquid state (CH₃OH, HCOOH) depending on the reaction conditions. Thus, the combination of selective reduction towards CO, high-efficiency conversion, and long-term stability of the photocatalysts remains challenging.

In this study, graphitic carbon nitride (g-C₃N₄) and covalent organic frameworks (COF) based on 4,4'-bipyridine and triazine in either exfoliated or bulk forms are evaluated for their ability to reduce gaseous CO₂ to CO in aqueous solutions through UV irradiation. The selection of the photocatalysts was based on two key factors: (i) the exfoliated carbon nitride has improved properties compared to the bulk carbon nitride [24–26] and (ii) the covalent organic framework consists of a triazine electron acceptor similar to carbon nitride; the triazine is moreover molecularly bonded to the bipyridine photosensitizer [27], which combines nitrogen cations and chlorine counter ions that are facilitating the polarization and adsorption of CO₂ molecules [20,28]. Triazine units as melam in g-C₃N₄ and melam in bCOF play their role in the photocatalytic mechanism by producing supplementary reactive sites of O₂^{•−} and h⁺ and OH[•] radicals, respectively, due to the differences in their electronic orbitals [29,30]. The exfoliated C₃N₄ was afterwards selected to serve as the template [26] for the in-situ growth of the covalent organic framework, creating new heterojunction materials at three different weight ratios through the nucleophilic substitution of the cyanuric chloride precursor with the unreacted amino groups of g-C₃N₄ [24,31]. All the organic photocatalysts were evaluated for their photocatalytic activity without any additions, promoting 100% selectivity towards CO. Finally, the potential photocatalysts were evaluated with the addition of Pt co-catalyst in order to ameliorate the reduction of CO₂ to CO. The differences in the photocatalytic performance of the prepared two-component heterojunction materials with different ratios were clarified.

2. Results and Discussion

2.1. Chemical and Structural Characterisation

The structure, morphology, and chemical composition of the g-C₃N₄ material and the bCOF have been previously described in references of Papailias et al. [25] and Bika et al. [32]. The FTIR spectra of the pristine and heterojunction materials with the three different ratios are presented in the order of (i) g-C₃N₄, (ii) HJ(1:10), (iii) HJ(1:1), (iv) HJ(10:1), and (v) bCOF, in Figure 1a (range: 500–2000 cm^{−1}) and Figure S2 (range: 400–4000 cm^{−1}). The substitution of the chlorine ions of cyanuric chloride by the highly exfoliated sheets of g-C₃N₄ and then by the 4,4'-bipyridine is validated by the absence of the C-Cl stretching vibration bond at 850 cm^{−1} for the HJ spectra (Figure 1a). The creation of -N-C-H between g-C₃N₄ and cyanuric chloride is further confirmed by the peak appearance at 2769 cm^{−1} of the HJ materials (Figure S2). Since the g-C₃N₄ and the bCOF are composed by similar carbon and nitrogen bonds, any further distinction in the HJ materials is challenging. The breathing mode of the triazine units is located at the range of 805–810 cm^{−1} depending on the triazine and heptazine configuration and the characteristic stretching of C-N, C=N heterocycles correspond to 1232–1629 cm^{−1}, observable in all HJ spectra (Figure S2). As the percentage of the COF increased though, these peaks in the HJ spectra became more distinct and intense. All vibrations are present in the HJ materials at the lower and higher frequencies. Additional =C-H bending and C-H stretching vibrations are traced at 530, 990, 3047 cm^{−1}, originating from the 4,4'-bipyridine units of bCOF and at 1408 cm^{−1} from g-C₃N₄. The shift of the C-N stretching at 1240 cm^{−1} and the decrease of its intensity is indicating a reaction between the terminal -N-H of g-C₃N₄ and the carbon atoms of the C₃N₃Cl₃ ring.

The slight differences observed in the chemical composition between the pristine and heterojunction materials are followed by the structural changes perceptible from the experimental powder X-ray diffraction patterns (Figure 1b). As previously reported [25], g-C₃N₄ is a semi-crystalline material, presenting its (002) plane of π-π stacking at 27.8° with a d spacing of 3.1 Å. The in-plane variation of the s-triazine structural motif exhibits a main peak at 12.1° with d spacing 7.3 Å (100). Unfortunately, this orientation is not distinguishable in the XRD pattern, as its repeatable chains are tangled due to the exfoliation process. On the other side, the bCOF is semi-crystalline with its main π-π stacking found at 26.9° with a 3.3 Å interlayer distance. Its organic network is characterized by different reflections as the one at 13.9° (6.2 Å) [22], the one of triazine at 12.1° (7.3 Å), and the one of 4,4 Bipyridine at 10.2° (8 Å). The viologen moieties can be periodically arranged with

certain spatial distances [33], exhibiting reflections between 20–25°, as seen later on at HJ and PM materials, where the COF content is dominant.

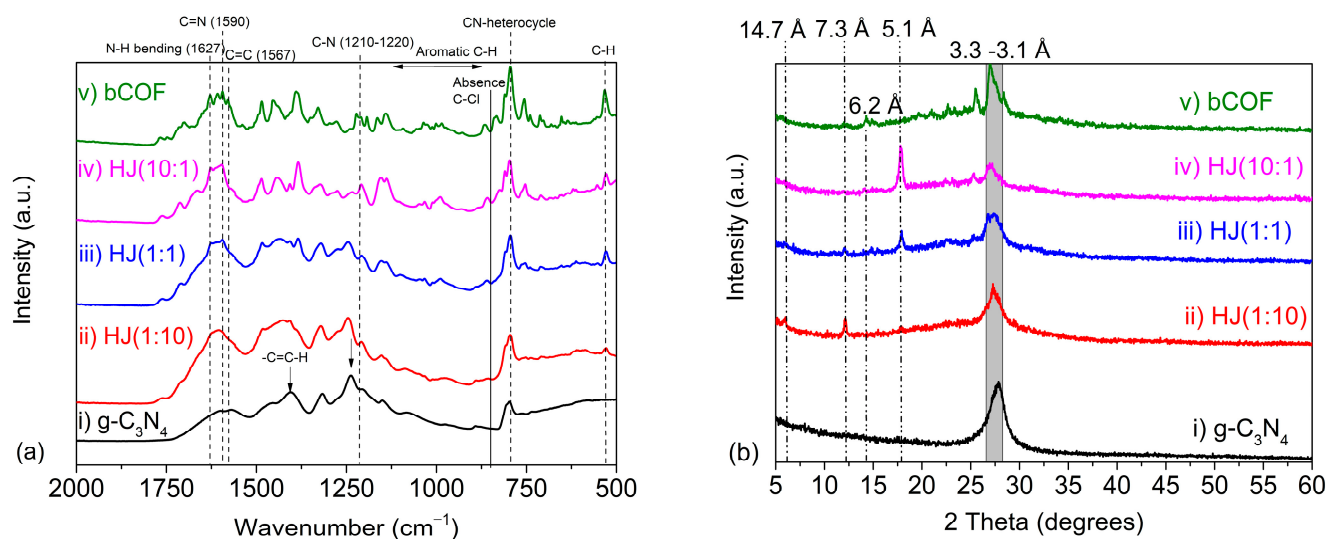


Figure 1. (a) FTIR and (b) XRD of the pristine (i,v) and heterojunction (ii,iii,iv) materials before the CO₂ photoreduction process.

At the XRD patterns of HJ materials, the π -conjugation between their layers causes the reflections to fluctuate between 26.9° and 27.8° (d-spacing of 3.3 and 3.1 Å) respectively, depending on the HJ weight ratio of g-C₃N₄ and COF. Overall, the increase in the amount of COF in the HJ materials initiated a shift of the characteristic (002) diffraction of g-C₃N₄. This shift is associated with the movement of the interlayer distance to larger d-spacing values, a decrease in its intensity, and a broadening of the FWHM. This occurred due to the growth of COF on the surface and boundaries of g-C₃N₄ layers and indicates the successful synthesis of the two-component HJ materials. In the HJ(1:1) and HJ(1:10), the (100) in-plane variation of the s-triazine structural motif found is also distinguishable at 12.1° with a repeating distance of 7.3 Å and its either the 2nd order diffraction of (200) at ~6° with a d-spacing of 14.7 Å or a modified distance between the s-triazine units of defected g-C₃N₄ assigned to (100) via HRTEM in C₃N₄ nanorods [34,35]. The latter can be based on structural rearrangements due to the reflux treatment. The peak becomes more evident as the g-C₃N₄ component content in HJs increases. Most importantly, a new sharp reflection is observed, augmenting gradually from HJ(1:10) to HJ(10:1) at 17.7° corresponding to a distance of 5 Å. Based on the bond lengths and by designing the structure of a repetitive HJ unit, the conclusion is that the distance of 5 Å corresponds from the center of the heptazine of g-C₃N₄ to the triazine of the COF. In Scheme 1, one of the repetitive units of the HJ materials is presented along with the new bond formed and the distance created and confirmed by the XRD pattern and the suitable bond lengths.

Further control experiments were performed to evaluate the new structural configurations that evolved thanks to the new covalent bond. Dispersions of the two semiconductors' physical mixtures were made as explained in Section 3.4, characterized, and their XRD patterns are presented in Figure S3. The two π -stacked components are forming the mixture through weak Van der Waals interactions and in contrast to the heterojunction materials the denoted characteristic diffraction at $2\theta = 17.7^\circ$ of the new bond is completely absent. After the inclusion of g-C₃N₄ layers, the diffraction peaks of the COF are modified, and reflections arise due to the alignment of its channels at 3.8° (2.3 nm) and 4.5° (1.95 nm) observed for the first time in this study in the PM(10:1). These peaks are hardly evident when the g-C₃N₄ content increases. Nevertheless, in the PM(1:1) and PM(1:10), the peaks at 6° and 12° are pronounced and their g-C₃N₄ origin is discussed in the previous paragraph.

Finally, AB staggered stacking peaks appear at 15° , while rearrangements of the viologen moieties inside the COFs reveal two reflections at 22° and 25° , as explained previously.



Scheme 1. (a) One of the proposed repetitive units of the heterojunction materials and the bond created between the nitrogen of $g\text{-C}_3\text{N}_4$ and the triazine of cyanuric chloride. The distance between the center of the closest heptazine in $g\text{-C}_3\text{N}_4$ and the center of the closest triazine in COF is calculated by the ChemDraw Software 16.0 at 5 Å. The $g\text{-C}_3\text{N}_4$ after its exfoliation contains -OH and =O groups. In the COF component, the three redox states (oxidative, radical, and reduced) of 4,4'-bipyridine are denoted. (b) The custom-made cylindrical stainless steel batch reactor used for the photocatalytic process.

The chemical and structural characterization conducted, verified the successful synthesis of the new HJ materials, also by identifying the covalent bond created between carbon nitride and cyanuric chloride.

2.2. Morphology before and after CO_2 Reduction

The morphology of the pristine materials before the photocatalytic process was demonstrated by SEM [25,32]. The bCOF has a layered irregularly shaped morphology, while the $g\text{-C}_3\text{N}_4$ has a sandwich-like morphology with an interconnected porous structure. In the prepared heterojunction materials presented in Figure 2, it is difficult to distinguish the

differences between the $g\text{-C}_3\text{N}_4$ and COF macroscopically. In the HJ(10:1) (Figure 2i), the photocatalyst is divided into small fragments, whereas the HJ(1:10) (Figure 2iii) consists of a larger porous sandwich-like structure originating from $g\text{-C}_3\text{N}_4$ and following its organization, and smaller non-homogeneously spread COF fragments. A similar morphology is met in HJ(1:1) (Figure 2ii) with the COF part more evenly represented. The COF is molecularly bonded on the $g\text{-C}_3\text{N}_4$ surface to obtain larger structures, making evident the strong interaction of both organic semiconductors. As far as the porosity is concerned, the nanoscopic differences cannot be observed by SEM.

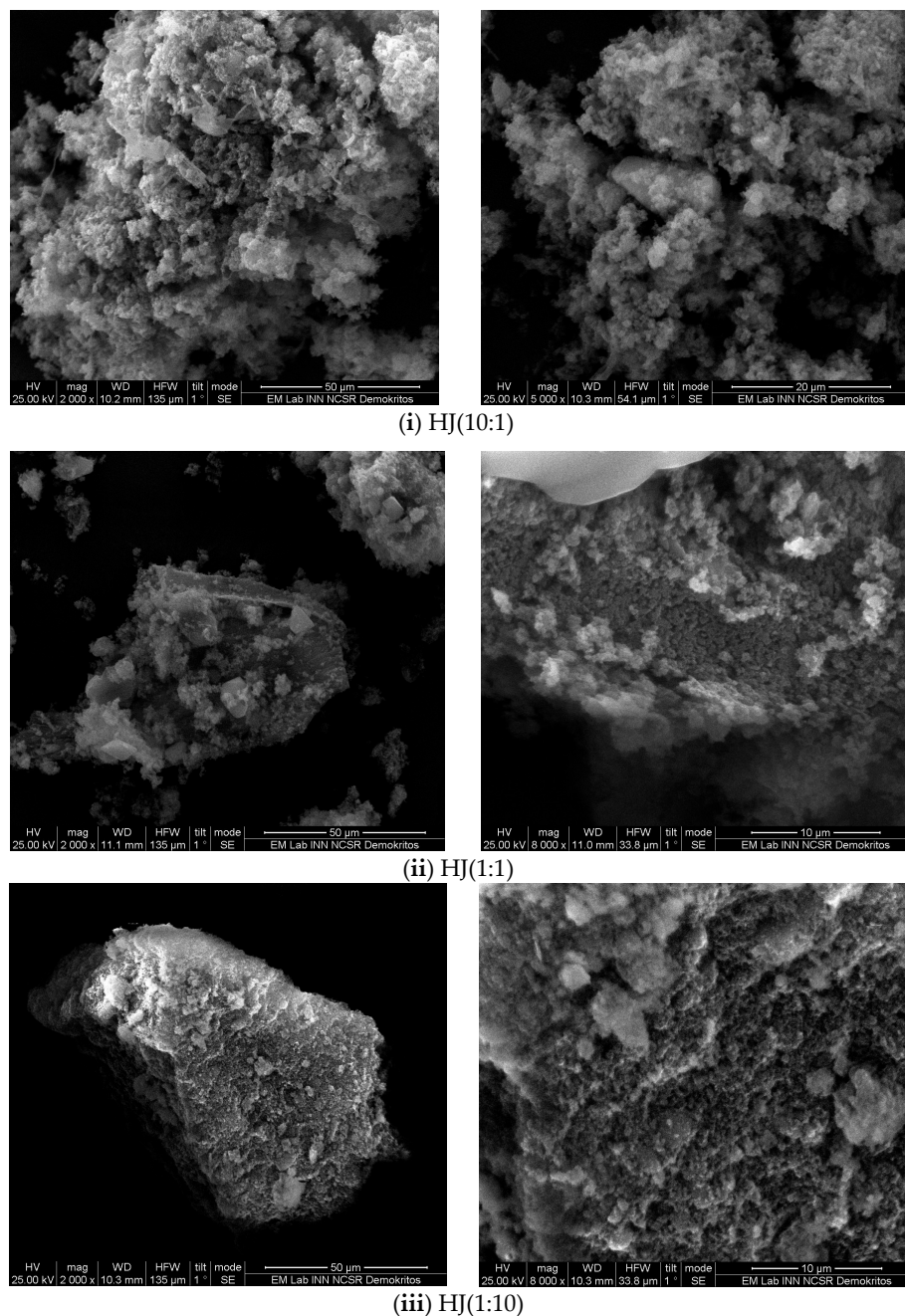


Figure 2. Morphology of the heterojunction materials before CO_2 reduction: (i) HJ(10:1), (ii) HJ(1:1), and (iii) HJ(1:10).

2.3. Photophysical Properties

The electronic structure of the semiconductors was examined through diffuse reflectance measurements (Figure S4). The spectra were plotted according to the Kubelka-

Munk function, and the Tauc-plots are displayed in Figure 3a taking into consideration a direct band gap with $n = 1/2$. Through extrapolation of the linear part of $(\alpha h\nu)^{1/n}$ vs. energy band gap (E_g), the corresponding values of g-C₃N₄ and bCOF are 3.04 eV and 2.75 eV, respectively.

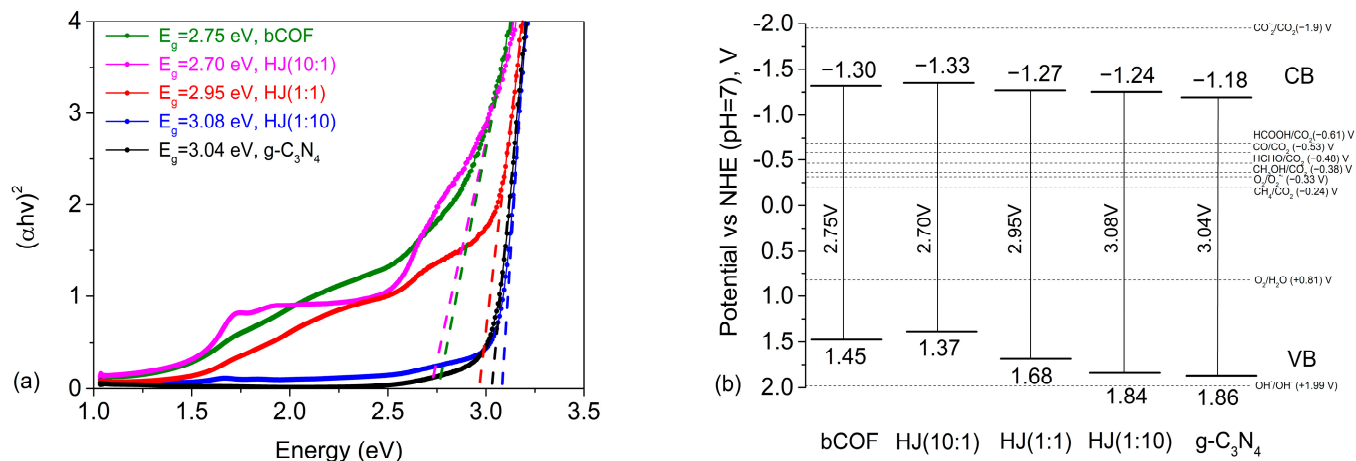


Figure 3. (a) Tauc-plots calculated from diffuse reflectance spectra for the estimation of the energy band gaps with direct transitions assumed in all cases. The intercept of the $(\alpha h\nu)^2$ versus (eV) plot provides the energy band gap of the materials and it is represented with dash lines. (b) The conduction/valence band edge potentials and band gap energies of the photocatalysts at pH = 7 vs. NHE with the redox potentials of the compounds involved in CO₂ photoreduction.

The same plots were performed for the HJ materials. The introduction of COF to the g-C₃N₄ modifies not only the morphological and structural properties but also the electronic and optical properties of the HJ materials. The band gap of the HJ photocatalysts is expanded starting from the 2.7 eV in HJ(10:1), rising to 2.96 eV for the HJ(1:1) till the highest value of 3.08 eV for HJ(1:10). Thus, modulating the ratio of the components in the HJ semiconductors, their band gap, as well as the reflection/absorption, can be adjusted. The decrease of the reflectance throughout the visible wavelength range is related to the increase of the COF component which possesses higher absorption at these wavelengths (Figure S4). In particular, the arrows in the grey highlighted areas at 450–460 nm and 650–750 nm in Figure S4, demonstrate the peaks that originate from the redox properties and the radicals of the COF [32] presented in the heterojunction materials. These peaks are more intense in the HJ(10:1) spectrum than in HJ(1:10) as the first one contains a higher COF content. In accordance, the composite HJ materials have a similar tendency, depending on their higher content component. For example, the HJ(1:10) reflects high percentages of visible light, as it contains a higher amount of g-C₃N₄ component which can be seen from its diffuse reflectance spectrum and its lighter green color than the other HJ materials (Figure S1).

The excitation-dependent photoluminescence maps of the 0.2 mg/mL photocatalysts' aqueous dispersions were measured to trace the emission of the semiconductors and to define their charge transport tendency. The PL maps of pristine and heterojunction semiconductors are presented in Figure S5. The excitation of the bCOF happens at 370–410 nm and its emission has a long Stokes shift and expands from 450 nm to 550 nm. For the g-C₃N₄, its excitation is found at 305 nm, its emission at 400 nm, and its intensity is stronger than the one of bCOF. The HJ(1:10) has a similar PL map to the g-C₃N₄. Regarding the other composites, the materials with greater or equal percentages of COF have their excitation shifted, creating two excitation centers at 325 nm and 375 nm for the HJ(1:1) and one center at 375 nm for the HJ(10:1). Their emission positions are found at 425 nm for the first one and at 430 nm for the latter one. Along with their new peaks [36], the intensity of photoluminescence decreases, as the content of COF in the heterojunction materials increases. This is indicative of the inhibition of the radiative recombination rate of electrons/holes,

improving the effective separation of charge carriers [26,31,36,37] and it can be correlated with better photocatalytic activity, as discussed afterward.

Electrochemical impedance measurements (Figure S6) defined the mobility of charge carriers in heterojunction semiconductors. Increased percentage of COF in the HJ materials, leads to decreased arc radius and this corresponds to an easier charge transport [18,26,31], in agreement with the PL measurements.

The Mott-Schottky approximation (Figure S7) was used to evaluate the position of the energy band edges and the type of semiconductors. The aim was to develop semiconductors thermodynamically suitable for the photocatalytic reduction of CO₂ to CO with H₂O assisting as a reductant, too [9,22]. To achieve this, the photocatalysts are required to have a lower conduction band (CB) potential compared to the CO₂ reduction potential (−0.53 V vs. NHE, pH = 7) and a higher valence band (VB) potential compared to the H₂O oxidation potential (+0.81 V vs. NHE, pH = 7). The mechanistic route that needs to be followed is mostly a series of multiple proton-coupled electron transfers, as CO₂ reduction requires high energy (−1.90 V) to be easily overpassed (Table S1).

Using Equation (1) combined with the values obtained from Mott-Schottky (Figure S9),

$$V_{CB} \sim V_{FB} (\text{NHE}; \text{pH} = 7) = V_{FB} (\text{Ag}/\text{AgCl}, \text{pH} 5.8) + \Delta V - 0.059 \times (7 - 5.8), \quad (1)$$

$$\Delta V = 0.21 \text{ and } V_{VB} = V_{CV} + E_g/e$$

and the results of the Tauc-plot (Figure 3a), the position of energy band edges are determined, gathered in Table S2, and presented in Figure 3b. In a physical simple mixing, the bCOF with g-C₃N₄ creates an organic type II system, where the photoinduced electrons of bCOF are transferred to g-C₃N₄ and the holes created are moving from g-C₃N₄ towards the bCOF. The energy band edges of the in-situ synthesized photocatalysts were also calculated in order to understand the influence of the different mass ratios of the constituents. They can be arranged in increasing order as follows: HJ(10:1) < bCOF < HJ(1:1) < g-C₃N₄ < HJ(1:10). Overall, the conduction and valence band edges of the HJ materials have slight differences: by increasing the g-C₃N₄ content in the HJ materials and thus the nitrogen content [16], the conduction band edge potential facilitates the photoinduced electrons transfer to the surface of the photocatalyst and then to the Pt co-catalyst in the case of a co-catalyst presence in the system [31,38]. Alongside the valence and conduction bands, Figure 3b demonstrates the necessary redox potentials of all the involved products of CO₂ photoreduction with these catalysts in an aqueous environment at pH = 7. Compared to reported heterojunction materials, the band gap of the pristine and the new HJ materials are similar or even larger than that of COF-modified g-C₃N₄ catalysts in [23,24,26,31,36,39–41]. As for their band edges, the conduction and valence band positions vary in the same potential range with the conductive band edge that has even more negative values compared to the catalysts in the mentioned works, depending on the ratio between the two components.

2.4. Photocatalytic Activity

The system and the photocatalytic procedure followed in this study are gathered in the Section 3.5 of Materials and Methods. The schematic representation of the setup is summarized in the graphical abstract and the calculations for the rate of the outlet gases are described in the supplementary material provided. The semiconductor is activated by light irradiation, the excitation leads to the formation of electrons in the conduction band and holes in the valence band. These sites are responsible for the photoreduction (e[−]) and the photooxidation (h⁺), respectively. The catalysts possess higher energy than the reduction potential of CO₂ and participate in the multiple-step reactions presented in Table S1. Meanwhile, the holes should be able to oxidize water to oxygen and protons, which are essential for photoreduction. All the synthesized photocatalysts in this study have their valence band at more positive potentials than the oxidation of water, providing the photodynamic conditions for CO₂.

2.4.1. Pristine Materials

The photocatalytic research commenced by evaluating the most common photocatalyst of titanium oxide (TiO_2), which serves as a reference point for the comparison of all the products' formation rates of the materials (Figure 4). The photocatalytic activity of TiO_2 towards CO_2 reduction in water was measured under the conditions of room temperature and UV light irradiation for 18 h without any sacrificial agent or co-catalyst and its rate of CO formation reached the value of $7.56 \mu\text{mol g}^{-1} \text{h}^{-1}$. Based on Papailias et al. [25], the two carbon nitride derivatives of melamine (bulk, $\text{b-C}_3\text{N}_4$, and chemically exfoliated, $\text{g-C}_3\text{N}_4$) have different energy band gaps, porosity, and surface areas. The exfoliated $\text{g-C}_3\text{N}_4$ revealed a higher porosity and specific surface area ($134.42 \text{ m}^2/\text{g}$) than $\text{b-C}_3\text{N}_4$ ($9 \text{ m}^2/\text{g}$) and it is expected to have higher formation rates of the CO_2 photoreduction products in water. For all these reasons, after the CO_2 reduction under UV irradiation for 18 h, the $\text{g-C}_3\text{N}_4$ demonstrated a $6.50 \mu\text{mol g}^{-1} \text{h}^{-1}$ CO rate close to the effectiveness of TiO_2 , in comparison to the $\text{b-C}_3\text{N}_4$ which produced CO with a low rate of $1.44 \mu\text{mol g}^{-1} \text{h}^{-1}$, in parallel with $177.6 \mu\text{mol g}^{-1} \text{h}^{-1}$ of the competitive H_2 evolution reaction (HER). Therefore, the exfoliated $\text{g-C}_3\text{N}_4$ photocatalyst was later used as the template for the in-situ synthesis of HJ materials, as it presented a higher CO formation rate with 100% selectivity in contrast to $\text{b-C}_3\text{N}_4$.

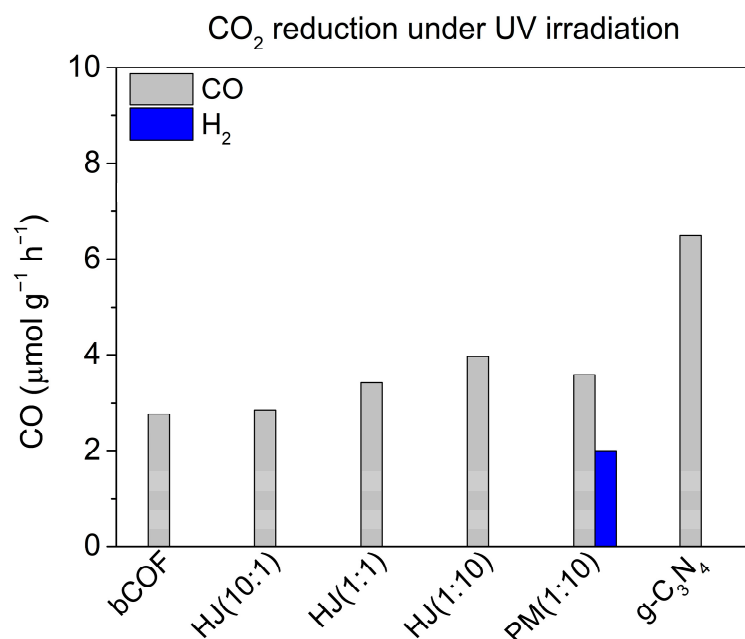


Figure 4. The CO and H_2 formation rates ($\mu\text{mol g}^{-1} \text{h}^{-1}$) of the pristine and heterojunction materials.

For the first time, the capacity of this bulk covalent organic framework (bCOF) to reduce CO_2 was evaluated and compared to the melamine derivatives (Figure 4). According to previous studies [25,32], the bCOF has a very low specific surface area ($4 \text{ m}^2/\text{g}$). Nevertheless, the bCOF is two times more efficient than the $\text{b-gC}_3\text{N}_4$, demonstrating a $2.77 \mu\text{mol g}^{-1} \text{h}^{-1}$ CO formation rate. The activity of the bCOF is similar to other modified carbon nitride materials [42]. This suggests that in this case, the surface area is not the most critical factor influencing photocatalytic performance as reported also by [43]. The latter is also related to the materials' electronic properties and photocatalytic active sites discussed below. Even though the bCOF has a lower surface area than the $\text{b-C}_3\text{N}_4$, it has superior charge carriers' mobility along its network, explaining the higher CO production rate.

Nonetheless, the exfoliated $\text{g-C}_3\text{N}_4$ has the highest rate of CO_2 to CO reduction among the pristine organic semiconductors, since it possesses a high surface area, radicals, and remaining active groups, promoting CO_2 reduction. Despite that, the optical and electronic properties of $\text{g-C}_3\text{N}_4$, its energy band gap, and its PL intensity are greater than the bCOF,

implying that it needs higher energy for its electrons to be excited to its CB and that it has a faster recombination rate.

As the photocatalytic systems in other reports include a different reactor, process, and calculations for the photocatalytic activity, the results can only qualitatively and approximately be compared. Hence, the $g\text{-C}_3\text{N}_4$ catalysts in the absence of sacrificial agents, co-catalysts, and under UV irradiation have a high CO production rate compared even to composite systems with TiO_2 [12,44]. For the bCOF, the CO production rate is lower than [19,45], though higher than [9], and similar to COFs with metal co-catalysts [20] and sacrificial agents [18] and to MOFs [7].

2.4.2. Heterojunction Materials

As the CO_2 photoreduction to CO was succeeded by both bCOF and $g\text{-C}_3\text{N}_4$ without any sacrificial agent or a co-catalyst, the activity of the new heterojunction materials is also evaluated and presented below. The CO formation rates are: $\text{HJ}(10:1) = 2.86 \mu\text{mol g}^{-1} \text{h}^{-1}$, $\text{HJ}(1:1) = 3.42 \mu\text{mol g}^{-1} \text{h}^{-1}$, $\text{HJ}(1:10) = 3.96 \mu\text{mol g}^{-1} \text{h}^{-1}$ (Figure 4). Thus, as the HJ materials reveal higher CO yields compared to the bCOF, there is a synergetic effect of the two-layered covalently bonded organic materials. Their efficiency is ameliorated by increasing their $g\text{-C}_3\text{N}_4$ content, even though it does not reach the photocatalytic activity of $g\text{-C}_3\text{N}_4$. This from a chemical perspective, may be due to the elimination of the unreacted amino or sulfide groups of $g\text{-C}_3\text{N}_4$, when it creates the heterojunction bond with the COF or due to the quicker charge transfer and recombination which originates from the materials' electronic properties as EIS, PL and UV-vis showed. Although charge separation is enhanced in $\text{HJ}(10:1)$ based on the EIS and PL measurements, its photocatalytic activity is limited contrary to the rest of $\text{HJ}(1:1)$ and $\text{HJ}(1:10)$, proposing that the COF or the $g\text{-C}_3\text{N}_4$ in the HJs is acting more as a photoactive center than a semiconductor leading to decreased performances [31]. The challenge was to increase the activity of COF with another carbon-based material and to adjust the synthesized heterojunction materials to the needs of this CO_2 reduction study towards selective CO production. For most of the reports with heterojunction or VdW catalysts of carbon nitride and covalent organic frameworks, catalysts are used for H_2 production [24,31,36,39]. A comparison can be made that the CO rate of the HJ catalysts is 100% selective but slightly lower than [26,40].

Overall, the migration direction of photo-induced electrons does not happen directly to the CO_2 molecules for the synthesized catalysts. A mechanistic pathway is assumed, where electrons photoexcited from the HOMO covering primarily the carbon nitride part migrate to the N-triazine moieties of the COF part (LUMO) through ICT and then transfer to the adsorbed CO_2 molecules. In the meantime, holes transport to the active sites of carbon nitride and oxidize the adsorbed H_2O to form O_2 and protons.

2.4.3. Pristine Materials in Physical Mixture

The $\text{HJ}(1:10)$ photocatalyst with the best performance among the new heterojunction materials was compared to the physical simple mixing $\text{PM}(1:10)$ of the two oppositely charged organic semiconductors, $g\text{-C}_3\text{N}_4$, and bCOF, with the ratio of (1:10) in H_2O . Its activity is displayed in Figure 4, along with the $\text{PM}(1:10)$ that demonstrated inferior catalytic performance of $3.58 \mu\text{mol g}^{-1} \text{h}^{-1}$ CO with the simultaneous competing evolution of $1.99 \mu\text{mol g}^{-1} \text{h}^{-1}$ H_2 , indicating that the intermolecular electron transfer is less efficient than the intramolecular interaction [16,36,40] between $g\text{-C}_3\text{N}_4$ and COF in the heterojunction material for the CO_2 photoreduction to CO. Although the $\text{PM}(1:10)$ is less effective and selective than $\text{HJ}(1:10)$, it offers a slightly better CO yield than bCOF, outlining the synergetic effect of COF and $g\text{-C}_3\text{N}_4$. On the other side, $g\text{-C}_3\text{N}_4$ loses its strong ability to reduce CO_2 in the presence of the bCOF in the $\text{PM}(1:10)$.

As Papailias et al. suggested [25], there are remaining functional groups in its networks that contain not only H but also OH which can promote H_2 production [46]. By reacting $g\text{-C}_3\text{N}_4$ with cyanuric chloride and then 4,4' bipyridine to create the heterojunction materials, the -N-H, -O-H of the $g\text{-C}_3\text{N}_4$ network are sacrificed in order to form covalent bonds with

the COF part. When the $g\text{-C}_3\text{N}_4$ semiconductor is combined in a physical mixture with the bCOF, a type II photocatalytic system is formed, where e^- and h^+ can migrate at ease. Thermodynamically, the barrier of the competitive H_2 evolution reaction is preferable to overpass as its redox potential of H_2 to H is -0.41 eV compared to the CO_2 to CO which is -0.51 eV. Furthermore, the VdW forces and p-p stacking interactions between the semiconductors block possibly the active sites responsible for the CO_2 to CO conversion, as this happens when the layers are stacked together at the bulk C_3N_4 .

2.4.4. Effect of Platinum Co-Catalyst

With the introduction of the H_2PtCl_6 in the aqueous dispersions of the photocatalysts, more efficient separation of the photogenerated electron-hole pairs is expected by an additional charge transfer process with its d-orbitals [47] and ligand-to-metal or metal-to-metal charge transfer effects [48]. The role of the co-catalyst is to decrease the activation energy facilitating the multi-electron pathway for CO_2 reduction [38].

The in-situ photodeposition of Pt has been verified to selectively approach specific sites of imine and pyridyl donors [48] near hydroxyl groups [49]. The catalytic sites are stabilized within the frameworks via confinement effects and coordination interactions [45]. Furthermore, COFs could modulate the coordination environment by changing their coordination group [45,48,50]. All things considered, it is beyond the scope of this study to conclude if all the amount of platinum is reduced to metallic particles, or a minor percentage creates complexes with the materials. The CO formation rates of the photocatalytic systems in the presence of Pt co-catalyst are illustrated in Figure 5. The co-catalyst in the bCOF dispersions has slightly improved the yield of the CO_2 conversion to $3.60 \mu\text{mol g}^{-1} \text{h}^{-1}$. Triazine with its electron-deficient character stabilizes the negative charges photo-generated on the COF and transfers them to the nearest platinum site leading to better activity [22,38]. However, the system reached its highest conversion with the addition of 5% H_2PtCl_6 , as the yield was constant until the amount of the co-catalyst on the bCOF dispersion was doubled (10%). High loadings of the co-catalyst in the photocatalytic systems do not favour the reactions due to the self-quenching of the excited states [48] and due to the light shielding by the presence of platinum [49].

On the contrary, the $g\text{-C}_3\text{N}_4$ is negatively influenced by the presence of platinum, activating its syngas ($\text{CO} + \text{H}_2$) production. The conversion rate of CO_2 to CO is reduced to $4.95 \mu\text{mol g}^{-1} \text{h}^{-1}$, while H_2 production rises to $1.41 \mu\text{mol g}^{-1} \text{h}^{-1}$ even with a small (0.1%) amount of 0.1% H_2PtCl_6 . Additionally, a higher percentage of H_2PtCl_6 was used (1%) and it was concluded that the sites of the co-catalyst on $g\text{-C}_3\text{N}_4$ are deactivated; its photocatalytic selectivity in conversion to CO is decreased substantially ($0.92 \mu\text{mol CO g}^{-1} \text{h}^{-1}$), while simultaneously the competitive H_2 evolution reaction is strongly promoted. Additionally, the increase in acidity of the dispersions with further addition of H_2PtCl_6 favours the production of protons and HER [28].

The attached COF on the surface and at the edges of $g\text{-C}_3\text{N}_4$ in the HJ photocatalysts alters and inhibits the tendency for HER of $g\text{-C}_3\text{N}_4$ in the presence of Pt co-catalyst. Based on [36], TEM demonstrated that platinum is mainly arranged on the COF and this outcome seems to suit well this study, as HJ materials follow the positive impact on their rates, similar to the Pt/bCOF system. The photoinduced electrons are transferred from the $g\text{-C}_3\text{N}_4$ to the COF and at the end to the platinum co-catalyst for the reduction of CO_2 . The photocatalytic efficiency of HJ(1:1) and HJ(1:10) are strongly improved to 4.14 and $7.56 \mu\text{mol CO g}^{-1} \text{h}^{-1}$, with the latter presenting superior efficiency among all the pristine and HJ materials, reaching the activity of TiO_2 . The exception is that the photocatalytic performance of HJ(10:1) is limited by the low 0.1% percent of the H_2PtCl_6 to $2.41 \mu\text{mol CO g}^{-1} \text{h}^{-1}$.

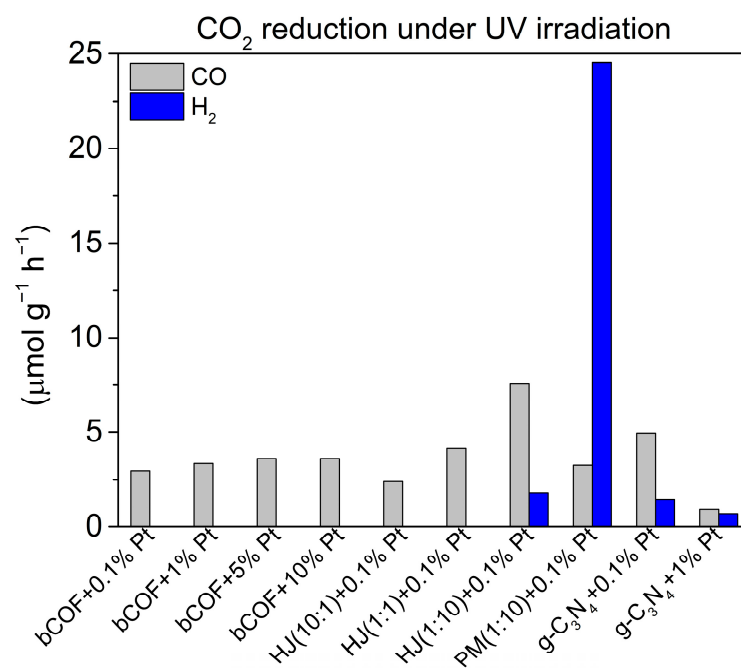


Figure 5. The CO and H₂ formation rates ($\mu\text{mol g}^{-1} \text{h}^{-1}$) of the pristine, heterojunction, and physical mixed materials in the presence of Pt co-catalyst.

Furthermore, the effect of the co-catalyst was evaluated for the physical mixture of (1:10). The addition of 0.1% H₂PtCl₆ to PM(1:10) led to the decrease of CO production to $3.24 \mu\text{mol g}^{-1} \text{h}^{-1}$ and the selective evolution of H₂ with an outstanding yield of $24.55 \mu\text{mol g}^{-1} \text{h}^{-1}$. This outcome contradicts the superior performance of HJ(1:10) with 0.1% H₂PtCl₆ towards the selective CO production. Thus, HJ materials are a vital proposition to many environmentally friendly applications and more precisely to those using carbon nitride photocatalysts with Pt to suppress H₂ production and benefit CO rates.

Overall, the photoreduction of CO₂ molecules is a complex electron transfer process. Under illumination, the organic frameworks absorb photons, and the excited electrons move to the catalytic active sites, including in the final stage the reduction site of Pt co-catalyst: this is based on a type II heterojunction mechanism where the migration of photoinduced e⁻ happens from the VB of the catalysts to the CB and then to the deposited Pt. CO₂ is temporarily absorbed on the surface, where the intermediate products are formed (Table S1), stabilized, and dissociated to CO or the competitive H₂ production along the case. Meanwhile, after the spatial separation, the photogenerated holes in the organic frameworks are capable of oxidizing H₂O to O₂ to balance electronically the photocatalytic system.

2.4.5. Sustainability and Control Experiments of the Pristine Materials

To assess a catalyst, the catalytic durability is important to evaluate. Each photocatalytic cycle follows the same procedure as CO₂ reduction described in Section 3.5. The dispersion undergoes purging of 20 min with Ar flow, before loading the reactor with CO₂ gas and letting the photocatalytic reaction proceed for 24 h. The outlet gas is analyzed by the GC at the end of each cycle and then the process is re-initialized with Ar flow to exclude the impact of the products produced in the previous cycle. The sustainability experiments of the pristine materials during 3 days of UV irradiation are shown in Figure 6 and demonstrated that both bCOF and g-C₃N₄ have lower CO rates from the 1st day. A possible explanation is that the organic networks had physisorbed on the surface molecules beneficial to CO₂ reduction that were desorbed with Ar bubbling. The g-C₃N₄ rate of CO kept changing during the repeated cycles, while H₂ was being produced due to the

occurrence of the competing proton reduction reactions. On the other side, the bCOF offered a constant rate with 100% selectivity towards CO.

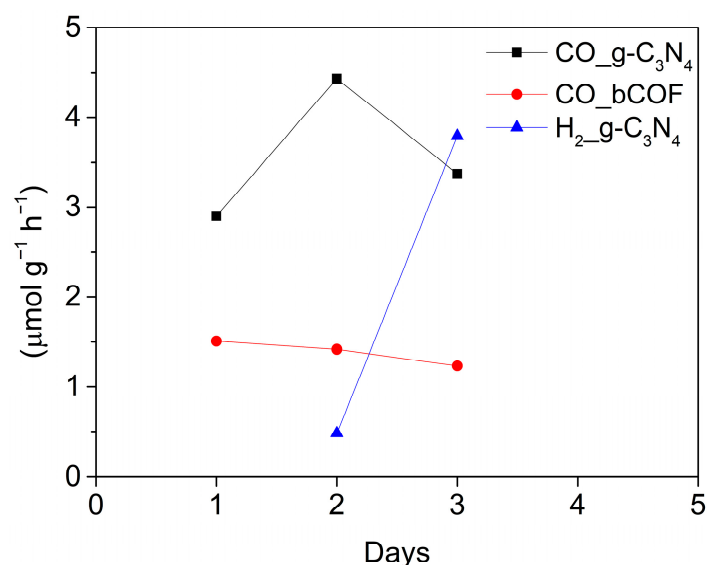


Figure 6. The 3 days sustainability cycles of the pristine g-C₃N₄ and bCOF.

The stability evaluation of the materials after the sustainability cycles was monitored by X-ray diffraction. The corresponding XRD patterns are displayed in Figure S8 and confirm that their structure remains largely unchanged. The bulk COF can delaminate when dispersed in water and a fraction was indeed observed at the centrifugation process, referred to in the paper as the supernatant (bCOFsup) after the CO₂ reduction. The π -stacking of both bCOF precipitate (bCOFprec) and bCOF(sup) supernatant is present, although with slightly decreased intensity and broadening of the FWHM. They present reflections deriving from viologen moieties at 10.2° (length of 4,4' Bipyridine units 8 Å) and at 20–25° (d-spacing 4.3–3.5 Å) where they are periodically arranged with certain spatial distances [33]. For g-C₃N₄, the diffraction peaks became more prominent after the photocatalytic process in water and more precisely the ones of 6.2° and 12° [34,35]. Generally, despite the remarkable photocatalytic performance of g-C₃N₄, in the long term, the bCOF is the stable platform of photocatalytic CO₂ to CO, as g-C₃N₄ loses its selectivity and benefits the H₂ evolution.

As a control experiment to uncover the carbon source of CO, the organic pristine semiconductors were dispersed in H₂O following the typical concentrations, and the batch reactor was purged and filled with argon, sealed, and illuminated with UV light. The GC measurements were collected after 18 h, as usual. Both samples presented amounts of desorbed gaseous CO₂, H₂, and CO, summarized in Table S3. The results either verify that the samples had already physisorbed CO₂ or that the continuous UV illumination led to the degradation of the materials. The XRD patterns (Figure S8) have shown for the bCOF and g-C₃N₄ that after the reduction process, there are no great alterations in their chemical or structural composition, indicating that there is no degradation of their networks. This leads to the conclusion that the photocatalysts had physisorbed CO₂ before their dispersion in water and maintained the physisorbed CO₂ quantity throughout the bubbling process with Ar. No visible degradation of the networks was observed after the photocatalytic process. The UV irradiation provided the necessary energy for a certain release and a small percentage had been also converted to the products of the reduction. Thus, the CO quantities after the photoreduction process indeed originate from the initially provided CO₂ gas into the batch reactor through the photocatalysts' activity.

With the purpose of having a fully integrated interpretation, their CO₂ uptake capacity and the isosteric heat of adsorption were measured. The CO₂ adsorption properties of bCOF and g-C₃N₄ were evaluated by measuring isotherms at various near-ambient temperatures

and pressures up to 20 bar using the gravimetric method. The corresponding excess isotherms are depicted in Figures S9 and S10, respectively. As expected, CO₂ uptake increases as the temperature decreases. G-C₃N₄ exhibits substantially higher CO₂ adsorbed amounts (1.89 mmol g⁻¹ at 0 °C, 20 bar) compared to the bCOF (0.42 mmol g⁻¹ at 0 °C, 20 bar). The results have a great correlation with the large difference observed in the samples' BET surface area, which was calculated to be 134.4 and 4.0 m² g⁻¹, respectively. Therefore, since g-C₃N₄ can retain more CO₂ on its surface, it is expected to perform more efficiently in the reduction reaction. Indeed, this suggestion was confirmed since the CO₂ uptake coincides with the yield of its photocatalytic reduction to CO.

CO₂ isosteric heats of adsorption (Q_{st}) as a function of surface coverage were extracted by applying the virial coefficients method to the measured isotherms [51] and the corresponding results are illustrated in Figure 7. Zero coverage isosteric heats of adsorption (Q_{st0}) were also calculated. bCOF demonstrates Q_{st0} equal to 25.94 kJ mol⁻¹ which is higher among others in the literature [52,53] and remains practically constant as surface coverage increases, indicative of a rather uniform potential landscape concerning adsorbate-surface interactions. The increased Q_{st} values can be a disadvantage since they translate to higher energy demands for CO₂ desorption and its subsequent conversion to CO. On the other hand, Q_{st0} was calculated to be 8.7 kJ mol⁻¹ for g-C₃N₄ and it rises to approximately 18 kJ mol⁻¹ with increasing surface coverage probably due to the formation of intermolecular forces between the adsorbate molecules.

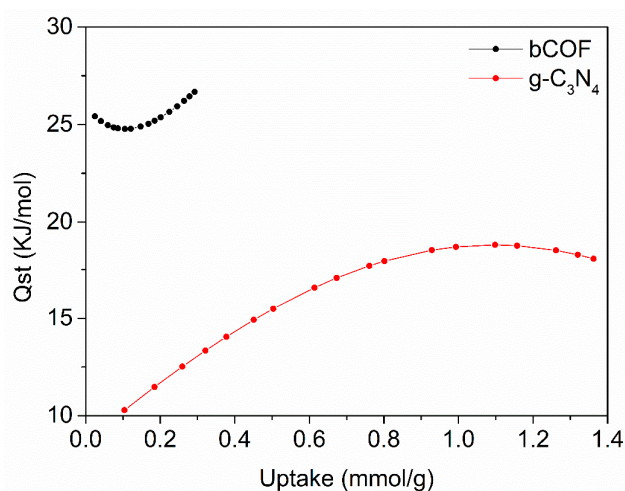


Figure 7. CO₂ isosteric heat of adsorption in bCOF and g-C₃N₄ as a function of surface coverage.

Thus, it is highlighted that even with a low CO₂ adsorption, the sites of the bCOF can produce stronger dipole-quadrupole intermolecular interaction with CO₂ [43] than g-C₃N₄, hindering the liberation of CO₂ from the surface and eventually its conversion to CO. This result would also explain that the bCOF over the photoreduction sustainability cycles maintained the rate of CO yield, without gaining any preferentiality towards H₂ production as g-C₃N₄ did.

In general, nitrogen can interact with polarizable CO₂ molecules via quadrupole-quadrupole interactions [53–55] and stabilize the negative charges to assist in the prolongation of the electron lifetimes [28]. Specifically, for carbon nitride materials, Shiraishi et al. [56,57] mention that formed e⁻ are localized at the C1 and N4 positions of the triazine ring of the melem structure, whereas the h⁺ are localized at the N2 and N6 positions. Recently, extended investigations of CO₂ adsorption on carbon nitride materials [58], highlight that the most preferable photocatalytic active site for CO₂ reduction is the nitrogen atom. Moreover, as the nitrogen atoms of the catalysts are capable of the capture of CO₂, the adsorption of H₂O physically or via hydrogen bonding interactions [28]. However, even though for the pristine material, the latter is possible, for the heterojunction materials

that form new delocalized π -conjugated systems, it would be difficult to distinguish the active sites without the aid of DFT theoretical studies.

Other adsorption sites of CO_2 can be the polar substituents of $-\text{NH}_2$ amine and $-\text{OH}$ groups that are mainly found in the photocatalysts in this study. The high interaction energy is also presented between the CO_2 and both Lewis acid and Lewis base sites. Furthermore, the chlorinated counterparts of bCOF contribute to the binding of CO_2 , owing to its ability to polarize CO_2 , similar to the fluorinated CONs [20]. The heat of sorption measurements provided a great potential of the COF-consistent photocatalyst of this study for their application in the gas separation field as well.

In the end, the new prominent heterojunction materials would combine the properties of the CO_2 uptake of $g\text{-C}_3\text{N}_4$ and the high isosteric heat of adsorption of bCOF, additionally to the hindering of the active sites responsible for HER during CO_2 reduction to CO.

3. Materials and Methods

3.1. Chemical Reagents

The chemical reagents cyanuric chloride (99.9%), toluene, and melamine were purchased from Sigma-Aldrich (St. Louis, MO, USA), and 4,4'-bipyridine (98%) was purchased from Alfa Aesar (Haverhill, MA, USA). The titanium oxide nanopowder (TiO_2 Degussa P25) and hexachloroplatinic acid (H_2PtCl_6) were provided by Sigma-Aldrich.

3.2. Photocatalysts

The procedure followed for the synthesis of bulk ($b\text{-C}_3\text{N}_4$) and chemically exfoliated ($g\text{-C}_3\text{N}_4$) carbon nitride materials are analytically presented in Papailias et al. [25], whereas the bulk COF (bCOF) was synthesized in accordance to Bika et al. [32]. Their powders have a white to yellow color for the carbon nitride derivatives [25] and green for the covalent organic framework [32].

3.3. Synthesis of Heterojunction Materials

A series of heterojunction composites of COF: $g\text{-C}_3\text{N}_4$ at a weight ratio of 10:1, 1:1, and 1:10, was in-situ synthesized, influenced by the work of Y. Xing et al. [36]. The method proceeds through the dispersion of the pre-synthesized $g\text{-C}_3\text{N}_4$ in toluene and the addition of a suitable amount of the cyanuric chloride and 4,4'-bipyridine precursors. Accordingly, the materials are denoted as HJ(10:1), HJ(1:1), and HJ(1:10). In a typical experiment for the synthesis of HJ(1:1), 80 mg of the chemically exfoliated $g\text{-C}_3\text{N}_4$ were subjected to ultrasonic treatment for 30 min in 20 mL toluene. Subsequently, 35.2 mg of cyanuric chloride in 5 mL toluene was added and the mixture was refluxed under magnetic stirring at 100–120 °C for 15 min to substitute the chlorine with the free N at the edges of the $g\text{-C}_3\text{N}_4$ layers. Afterwards, 44.8 mg of 4,4'-bipyridine in 5 mL toluene was added and left to react with the mixture at 180 °C for 24 h. The powder was collected by filtration, washed with toluene, and dried at room temperature. The synthesis of the HJ(10:1) and the HJ(1:10) materials followed the same procedure with the appropriate amounts and the pertinent powdered samples are displayed in Figure S1. The color of the materials (dark green for HJ(10:1) and light green for HJ(1:10)) is the first indication that both components exist in the HJs. The proposed repetitive unit of the synthesized heterojunction materials is presented in Scheme 1a. The amounts of the precursors for the synthesis of HJ(10:1) and HJ(1:10) were accordingly estimated, however, all the heterojunction materials had a yield of 60%.

3.4. Physical Mixing

The simple process of the physical mixing of the two organic layers includes the dispersion and sonication for 30 min of 4 mg of bCOF and 40 mg of $g\text{-C}_3\text{N}_4$ in 100 mL aqueous solution to create the physical mix of (1:10) ratio, denoted as PM(1:10). Two more samples were prepared with a physical mixing process denoted as PM(10:1) and PM(1:1).

3.5. Photocatalytic Reduction

A custom-made cylindrical stainless steel batch reactor (Scheme 1b) with an 8 cm height and 6.5 cm diameter was employed for the photocatalytic experiments. The reactor is separated into two sections; the first with a volume of 100 mL is where the catalysts are dispersed and the second, occupies 4 cm height and the free space of 3.3 cm where the CO₂ gas is stored. A pressure indicator was integrated to monitor the current pressure in the reactor. An admit valve was incorporated for the high-purity CO₂ (99.998%) and Ar (99.995%) supply into the reactor and an exhaust valve was used to connect the system with the Gas chromatograph. The CO₂ reduction process starts with the dilution and sonication of a 40 mg catalyst in 100 mL of deionized water. A magnetic stirrer is added to the reactor along with the dispersion. To ensure the removal of any contaminants from the reaction atmosphere, the dispersion is purged with a continuous CO₂ gas flow for 20 min while the pressure in the reactor is kept stable at 1.5 bar. Afterwards, the reactor is filled with CO₂ at a constant pressure of 1.75 bar and sealed for the heterogeneous photocatalytic reaction. The photocatalytic activity of the catalysts' aqueous dispersions was measured under UV-A irradiation (Philips Cleo Compact 15 W Lamps) with an intensity of 9 W/m² at room temperature. The resulting amounts of the CO₂ reduction products were monitored by a GC-2010 Shimadzu gas chromatograph equipped with a BID-2010 detector and they were quantified by the corresponding software. The calculations for the formation rate in $\mu\text{mol g}^{-1} \text{h}^{-1}$ are described at the end of the Supplementary Materials.

3.6. Characterization Techniques

Fourier Transform Infrared (FTIR) spectra for the samples in the solid state were measured on a Thermo Nicolet iS50 instrument in attenuated total reflection mode from 400 cm⁻¹ to 4000 cm⁻¹. X-ray diffraction (XRD) patterns were completed in the 2 θ range of 2–60° with a Siemens D500 X-ray diffractometer, using Cu-K_a radiation ($\lambda = 1.5418 \text{ \AA}$) for solid powders and films deposited on glass substrates. Scanning electron microscopy (SEM) by FEI inspect microscope equipped with tungsten filament operating at 25 kV was used to investigate the morphology of the semiconducting powders, which were sputter-coated with Au beforehand. The electrochemical behaviour of the prepared materials was evaluated using a Metrohm Autolab PGSTAT302 potentiometer in conjunction with a beaker-type three-electrode cell. For the measurements, counter (Pt sheet), reference (Ag/AgCl, 3 M KCl), and working (Glassy carbon covered with 25 μL of the investigated material) electrodes were embedded into a 0.2 M Na₂SO₄ electrolyte solution (pH \sim 5.8); the electrode material was prepared based on Giannakopoulou et al. [59]. The Mott–Schottky plots were recorded at potentials from -1.3 V to -0.9 V with perturbations of the same amplitude of 0.01 V for the frequencies of 100 Hz, 316 Hz, and 1000 Hz. Uv-Vis diffuse reflectance and absorbance spectra were carried out on a Specord Analytik Jena 210+ spectrophotometer with quartz cuvettes of 10 mm path length. Excitation-dependent photoluminescence (PL) spectra were obtained using a JASCO FP-8300 spectrofluorometer. The sensitivity was set at a low level for these measurements. The photocatalytic measurements were conducted on a GC-2010 Shimadzu gas chromatograph with the Carboxen[®]-1010 PLOT and equipped with a BID-2010 detector. CO₂ excess adsorption isotherms were measured at various near-ambient temperatures and pressures up to 20 bar on an intelligent gravimetric analyzer (IGA-001, Hidden Isochema, Warrington, UK).

4. Conclusions

In this work, the synthesis, characterization, and photocatalytic application towards CO₂ reduction for a series of pristine covalent organic frameworks, exfoliated carbon nitride, and their unique heterojunctions were presented. The new molecular bond was successfully identified by X-ray diffraction and FTIR spectroscopy. The prominent heterojunction photocatalysts owe the positive aspects of each constituent for effective, selective CO₂ capture and selective photoreduction to CO. The optimum ratio between the two organic components was identified and the effect of Pt co-catalyst on the selective CO production

was thoroughly examined. Although the co-catalyst had a positive impact on the CO yield of the COF-based photocatalysts, it had a negative influence on the g-C₃N₄ photocatalyst, by enhancing H₂ evolution. The unique interface between the two semiconductors at (1:10) heterojunction with the addition of 0.1% H₂PtCl₆ led to improved photocatalytic activity towards CO, preventing the competitive H₂ evolution reaction. Furthermore, the creation of the intramolecular bond between COF and g-C₃N₄ was beneficial to the photoreduction process in comparison to their physical mixture, which promoted instead a significant evolution of H₂ when platinum was present in the photocatalytic system.

Supplementary Materials: The following supporting information can be downloaded at: <https://www.mdpi.com/article/10.3390/catal13101331/s1>. FTIR spectra, XRD patterns, SEM images, diffuse reflectance spectra, excitation-dependent photoluminescence mapping, Mott-Schottky plots, CO₂ sorption isotherms, and CO₂ isosteric heat of adsorption plots are available free of charge via the internet.

Author Contributions: Conceptualization, P.B., I.P. and P.D.; Methodology, P.B., I.P. and P.D.; Software, P.B.; Validation, all authors.; Formal Analysis, P.B., I.P., T.G. and C.T. (Christos Tampaxis); Investigation, P.B., I.P., T.G. and P.D.; Resources, C.T. (Christos Trapalis) and P.D.; Data Curation, P.B.; Writing—Original Draft Preparation, P.B.; Writing—Review & Editing, P.B., I.P., T.G. and P.D.; Visualization, P.B., I.P. and P.D.; Supervision, T.A.S., C.T. (Christos Trapalis) and P.D.; Project Administration, P.D.; Funding Acquisition, T.A.S., C.T. (Christos Trapalis) and P.D. All authors have read and agreed to the published version of the manuscript.

Funding: P.D. and P.B. acknowledge the Hellenic Foundation for Research and Innovation and the General Secretariat for Research and Innovation (grant number: PLASCAT 1468). The financial support from the “ATTP4-0349671 APOGEION” (MIS 5185024) project co-financed by the European Union and Greek National Funds through the Operational Program ATTIKA 2014–2020, under the call RESEARCH AND INNOVATION COOPERATIONS IN THE REGION OF ATTICA is appreciated.

Data Availability Statement: Most data acquired for this manuscript are summarized in the Supplementary Materials. All other data can be obtained at the request of the corresponding author.

Conflicts of Interest: The authors declare no conflict of interest.

References

1. He, Y.; Peng, G.; Jiang, Y.; Zhao, M.; Wang, X.; Chen, M.; Lin, S. Environmental Hazard Potential of Nano-Photocatalysts Determined by Nano-Bio Interactions and Exposure Conditions. *Small* **2020**, *16*, 1907690. [CrossRef]
2. Rueda-Marquez, J.J.; Levchuk, I.; Fernández Ibañez, P.; Sillanpää, M. A Critical Review on Application of Photocatalysis for Toxicity Reduction of Real Wastewaters. *J. Clean. Prod.* **2020**, *258*, 120694. [CrossRef]
3. Zhang, J.; Pham, T.H.M.; Ko, Y.; Li, M.; Yang, S.; Koolen, C.D.; Zhong, L.; Luo, W.; Züttel, A. Tandem Effect of Ag@C@Cu Catalysts Enhances Ethanol Selectivity for Electrochemical CO₂ Reduction in Flow Reactors. *Cell Rep. Phys. Sci.* **2022**, *3*, 100949. [CrossRef]
4. Zhang, Y.; Wang, Y.; Guo, C.; Wang, Y. Molybdenum Carbide-Based Photocatalysts: Synthesis, Functionalization, and Applications. *Langmuir* **2022**, *38*, 12739–12756. [CrossRef] [PubMed]
5. Wang, W.-N.; Soulis, J.; Yang, Y.J.; Biswas, P. Comparison of CO₂ Photoreduction Systems: A Review. *Aerosol Air Qual. Res.* **2014**, *14*, 533–549. [CrossRef]
6. Chang, X.; Wang, T.; Gong, J. CO₂ Photo-Reduction: Insights into CO₂ Activation and Reaction on Surfaces of Photocatalysts. *Energy Environ. Sci.* **2016**, *9*, 2177–2196. [CrossRef]
7. Li, R.; Zhang, W.; Zhou, K. Metal–Organic-Framework-Based Catalysts for Photoreduction of CO₂. *Adv. Mater.* **2018**, *30*, 1705512. [CrossRef]
8. Chen, J.; Tao, X.; Li, C.; Ma, Y.; Tao, L.; Zheng, D.; Zhu, J.; Li, H.; Li, R.; Yang, Q. Synthesis of Bipyridine-Based Covalent Organic Frameworks for Visible-Light-Driven Photocatalytic Water Oxidation. *Appl. Catal. B Environ.* **2020**, *262*, 118271. [CrossRef]
9. Lu, M.; Liu, J.; Li, Q.; Zhang, M.; Liu, M.; Wang, J.; Yuan, D.; Lan, Y. Rational Design of Crystalline Covalent Organic Frameworks for Efficient CO₂ Photoreduction with H₂O. *Angew. Chem.* **2019**, *131*, 12522–12527. [CrossRef]
10. Chen, R.; Wang, Y.; Ma, Y.; Mal, A.; Gao, X.Y.; Gao, L.; Qiao, L.; Li, X.B.; Wu, L.Z.; Wang, C. Rational Design of Isostructural 2D Porphyrin-Based Covalent Organic Frameworks for Tunable Photocatalytic Hydrogen Evolution. *Nat. Commun.* **2021**, *12*, 1354. [CrossRef]
11. Cao, S.; Yu, J. Journal of Photochemistry and Photobiology C : Photochemistry Reviews Carbon-Based H₂-Production Photocatalytic Materials. *J. Photochem. Photobiol. C Photochem. Rev.* **2016**, *27*, 72–99. [CrossRef]
12. Wen, J.; Xie, J.; Chen, X.; Li, X. A Review on G-C₃N₄ -Based Photocatalysts. *Appl. Surf. Sci.* **2017**, *391*, 72–123. [CrossRef]

13. Yang, Q.; Luo, M.; Liu, K.; Cao, H.; Yan, H. Covalent Organic Frameworks for Photocatalytic Applications. *Appl. Catal. B Environ.* **2020**, *276*, 119174. [[CrossRef](#)]
14. Geng, Q.; Xu, Z.; Wang, J.; Song, C.; Wu, Y.; Wang, Y. Tailoring Covalent Triazine Frameworks Anode for Superior Lithium-Ion Storage via Thioether Engineering. *Chem. Eng. J.* **2023**, *469*, 143941. [[CrossRef](#)]
15. Pan, J.; Guo, L.; Zhang, S.; Wang, N.; Jin, S.; Tan, B. Embedding Carbon Nitride into a Covalent Organic Framework with Enhanced Photocatalysis Performance. *Chem. Asian J.* **2018**, *13*, 1674–1677. [[CrossRef](#)]
16. Yao, Y.; Hu, Y.; Hu, H.; Chen, L.; Yu, M.; Gao, M.; Wang, S. Metal-Free Catalysts of Graphitic Carbon Nitride–Covalent Organic Frameworks for Efficient Pollutant Destruction in Water. *J. Colloid Interface Sci.* **2019**, *554*, 376–387. [[CrossRef](#)]
17. Wang, X.; Gong, J.; Dong, Y.; An, S.; Zhang, X.; Tian, J. Energy Band Engineering of Hydroxyethyl Group Grafted on the Edge of 3D G-C₃N₄ Nanotubes for Enhanced Photocatalytic H₂ Production. *Mater. Today Phys.* **2022**, *27*, 100806. [[CrossRef](#)]
18. Zhong, H.; Hong, Z.; Yang, C.; Li, L.; Xu, Y.; Wang, X.; Wang, R. A Covalent Triazine-Based Framework Consisting of Donor–Acceptor Dyads for Visible-Light-Driven Photocatalytic CO₂ Reduction. *ChemSusChem* **2019**, *12*, 4493–4499. [[CrossRef](#)]
19. Liu, W.; Li, X.; Wang, C.; Pan, H.; Liu, W.; Wang, K.; Zeng, Q.; Wang, R.; Jiang, J. A Scalable General Synthetic Approach toward Ultrathin Imine-Linked Two-Dimensional Covalent Organic Framework Nanosheets for Photocatalytic CO₂ Reduction. *J. Am. Chem. Soc.* **2019**, *141*, 17431–17440. [[CrossRef](#)]
20. Wang, X.; Fu, Z.; Zheng, L.; Zhao, C.; Wang, X.; Chong, S.Y.; McBride, F.; Raval, R.; Bilton, M.; Liu, L.; et al. Covalent Organic Framework Nanosheets Embedding Single Cobalt Sites for Photocatalytic Reduction of Carbon Dioxide. *Chem. Mater.* **2020**, *32*, 9107–9114. [[CrossRef](#)]
21. Ran, L.; Li, Z.; Ran, B.; Cao, J.; Zhao, Y.; Shao, T.; Song, Y.; Leung, M.K.H.; Sun, L.; Hou, J. Engineering Single-Atom Active Sites on Covalent Organic Frameworks for Boosting CO₂ Photoreduction. *J. Am. Chem. Soc.* **2022**, *144*, 17097–17109. [[CrossRef](#)] [[PubMed](#)]
22. Fu, Y.; Zhu, X.; Huang, L.; Zhang, X.; Zhang, F.; Zhu, W. Azine-Based Covalent Organic Frameworks as Metal-Free Visible Light Photocatalysts for CO₂ Reduction with H₂O. *Appl. Catal. B Environ.* **2018**, *239*, 46–51. [[CrossRef](#)]
23. Li, X.; Yu, J.; Jaroniec, M.; Chen, X. Cocatalysts for Selective Photoreduction of CO₂ into Solar Fuels. *Chem. Rev.* **2019**, *119*, 3962–4179. [[CrossRef](#)] [[PubMed](#)]
24. Luo, M.; Yang, Q.; Yang, W.; Wang, J.; He, F.; Liu, K.; Cao, H.; Yan, H. Defects Engineering Leads to Enhanced Photocatalytic H₂ Evolution on Graphitic Carbon Nitride–Covalent Organic Framework Nanosheet Composite. *Small* **2020**, *16*, 2001100. [[CrossRef](#)] [[PubMed](#)]
25. Papailias, I.; Todorova, N.; Giannakopoulou, T.; Ioannidis, N.; Boukos, N.; Athanasekou, C.P.; Dimotikali, D.; Trapalis, C. Chemical vs Thermal Exfoliation of G-C₃N₄ for NO_x Removal under Visible Light Irradiation. *Appl. Catal. B Environ.* **2018**, *239*, 16–26. [[CrossRef](#)]
26. Song, X.; Wu, Y.; Zhang, X.; Li, X.; Zhu, Z.; Ma, C.; Yan, Y.; Huo, P.; Yang, G. Boosting Charge Carriers Separation and Migration Efficiency via Fabricating All Organic van Der Waals Heterojunction for Efficient Photoreduction of CO₂. *Chem. Eng. J.* **2021**, *408*, 127292. [[CrossRef](#)]
27. Bourlinos, A.B.; Dallas, P.; Sanakis, Y.; Stamopoulos, D.; Trapalis, C.; Niarchos, D. Synthesis and Characterization of a π -Conjugate, Covalent Layered Network Derived from Condensation Polymerization of the 4,4'-Bipyridine-Cyanuric Chloride Couple. *Eur. Polym. J.* **2006**, *42*, 2940–2948. [[CrossRef](#)]
28. Lei, K.; Wang, D.; Ye, L.; Kou, M.; Deng, Y.; Ma, Z.; Wang, L.; Kong, Y. A Metal-Free Donor–Acceptor Covalent Organic Framework Photocatalyst for Visible-Light-Driven Reduction of CO₂ with H₂O. *ChemSusChem* **2020**, *13*, 1725–1729. [[CrossRef](#)]
29. Liu, N.; Li, T.; Zhao, Z.; Liu, J.; Luo, X.; Yuan, X.; Luo, K.; He, J.; Yu, D.; Zhao, Y. From Triazine to Heptazine: Origin of Graphitic Carbon Nitride as a Photocatalyst. *ACS Omega* **2020**, *5*, 12557–12567. [[CrossRef](#)]
30. Ye, H.; Gong, N.; Cao, Y.; Fan, X.; Song, X.; Li, H.; Wang, C.; Mei, Y.; Zhu, Y. Insights into the Role of Protonation in Covalent Triazine Framework-Based Photocatalytic Hydrogen Evolution. *Chem. Mater.* **2022**, *34*, 1481–1490. [[CrossRef](#)]
31. Luo, M.; Yang, Q.; Liu, K.; Cao, H.; Yan, H. Boosting Photocatalytic H₂ Evolution on G-C₃N₄ by Modifying Covalent Organic Frameworks (COFs). *Chem. Commun.* **2019**, *55*, 5829–5832. [[CrossRef](#)] [[PubMed](#)]
32. Bika, P.; Giannakopoulou, T.; Osokin, V.; Li, M.; Todorova, N.; Kaidatzis, A.; Taylor, R.A.; Trapalis, C.; Dallas, P. An Insight Study into the Parameters Altering the Emission of a Covalent Triazine Framework. *J. Mater. Chem. C* **2021**, *9*, 13770–13781. [[CrossRef](#)]
33. Zhang, Y.; Zhang, K.; Wu, L.; Liu, K.; Huang, R.; Long, Z.; Tong, M.; Chen, G. Facile Synthesis of Crystalline Viologen-Based Porous Ionic Polymers with Hydrogen-Bonded Water for Efficient Catalytic CO₂ Fixation under Ambient Conditions. *RSC Adv.* **2020**, *10*, 3606–3614. [[CrossRef](#)]
34. Sun, B.W.; Yu, H.Y.; Yang, Y.J.; Li, H.J.; Zhai, C.Y.; Qian, D.J.; Chen, M. New Complete Assignment of X-Ray Powder Diffraction Patterns in Graphitic Carbon Nitride Using Discrete Fourier Transform and Direct Experimental Evidence. *Phys. Chem. Chem. Phys.* **2017**, *19*, 26072–26084. [[CrossRef](#)] [[PubMed](#)]
35. Bai, X.; Wang, L.; Zong, R.; Zhu, Y. Photocatalytic Activity Enhanced via G-C₃N₄ Nanoplates to Nanorods. *J. Phys. Chem. C* **2013**, *117*, 9952–9961. [[CrossRef](#)]
36. Xing, Y.; Yin, L.; Zhao, Y.; Du, Z.; Tan, H.Q.; Qin, X.; Ho, W.; Qiu, T.; Li, Y.G. Construction of the 1D Covalent Organic Framework/2D g-C₃N₄ Heterojunction with High Apparent Quantum Efficiency at 500 Nm. *ACS Appl. Mater. Interfaces* **2020**, *12*, 51555–51562. [[CrossRef](#)] [[PubMed](#)]

37. Gopalakrishnan, V.N.; Nguyen, D.T.; Becerra, J.; Sakar, M.; Ahad, J.M.E.; Jautzy, J.J.; Mindorff, L.M.; Béland, F.; Do, T.O. Manifestation of an Enhanced Photoreduction of CO₂ to CO over the in Situ Synthesized RGO-Covalent Organic Framework under Visible Light Irradiation. *ACS Appl. Energy Mater.* **2021**, *4*, 6005–6014. [[CrossRef](#)]
38. Vyas, V.S.; Haase, F.; Stegbauer, L.; Savasci, G.; Podjaski, F.; Ochsenfeld, C.; Lotsch, B.V. A Tunable Azine Covalent Organic Framework Platform for Visible Light-Induced Hydrogen Generation. *Nat. Commun.* **2015**, *6*, 8508. [[CrossRef](#)]
39. Liu, Y.; Jiang, L.; Tian, Y.; Xu, Z.; Wang, W.; Qiu, M.; Wang, H.; Li, X.; Zhu, G.; Wang, Y. Covalent Organic Framework/g-C₃N₄ van Der Waals Heterojunction toward H₂ Production. *Inorg. Chem.* **2023**, *62*, 3271–3277. [[CrossRef](#)]
40. Pan, Z.; Niu, P.; Liu, M.; Zhang, G.; Zhu, Z.; Wang, X. Molecular Junctions on Polymeric Carbon Nitrides with Enhanced Photocatalytic Performance. *ChemSusChem* **2020**, *13*, 888–892. [[CrossRef](#)]
41. Shahbazi, H.; Shafei, A.; Sheibani, S. The Effect of Carbon Nanotubes Functionalization on the Band-Gap Energy of TiO₂-CNT Nanocomposite. *AIP Conf. Proc.* **2018**, *1920*, 020040. [[CrossRef](#)]
42. Oh, Y.; Le, V.D.; Maiti, U.N.; Hwang, J.O.; Park, W.J.; Lim, J.; Lee, K.E.; Bae, Y.S.; Kim, Y.H.; Kim, S.O. Selective and Regenerative Carbon Dioxide Capture by Highly Polarizing Porous Carbon Nitride. *ACS Nano* **2015**, *9*, 9148–9157. [[CrossRef](#)] [[PubMed](#)]
43. Li, Z.; Zhi, Y.; Feng, X.; Ding, X.; Zou, Y.; Liu, X.; Mu, Y. An Azine-Linked Covalent Organic Framework: Synthesis, Characterization and Efficient Gas Storage. *Chem. Eur. J.* **2015**, *21*, 12079–12084. [[CrossRef](#)] [[PubMed](#)]
44. Chen, Y.; Jia, G.; Hu, Y.; Fan, G.; Tsang, Y.H.; Li, Z.; Zou, Z. Two-Dimensional Nanomaterials for Photocatalytic CO₂ Reduction to Solar Fuels. *Sustain. Energy Fuels* **2017**, *1*, 1875–1898. [[CrossRef](#)]
45. Zhong, W.; Sa, R.; Li, L.; He, Y.; Li, L.; Bi, J.; Zhuang, Z.; Yu, Y.; Zou, Z. A Covalent Organic Framework Bearing Single Ni Sites as a Synergistic Photocatalyst for Selective Photoreduction of CO₂ to CO. *J. Am. Chem. Soc.* **2019**, *141*, 7615–7621. [[CrossRef](#)] [[PubMed](#)]
46. Todorova, N.; Papailias, I.; Giannakopoulou, T.; Ioannidis, N.; Boukos, N.; Dallas, P.; Edelmannová, M.; Reli, M.; Kočí, K.; Trapalis, C. Photocatalytic H₂ evolution, CO₂ reduction, and Noxoxidation by Highly Exfoliated g-C₃N₄. *Catalysts* **2020**, *10*, 1147. [[CrossRef](#)]
47. López-Magano, A.; Platero-Prats, A.E.; Cabrera, S.; Mas-Ballesté, R.; Alemán, J. Incorporation of Photocatalytic Pt(II) Complexes into Imine-Based Layered Covalent Organic Frameworks (COFs) through Monomer Truncation Strategy. *Appl. Catal. B Environ.* **2020**, *272*, 119027. [[CrossRef](#)]
48. Almansaf, Z.; Hu, J.; Zanca, F.; Shahsavari, H.R.; Kampmeyer, B.; Tsuji, M.; Maity, K.; Lomonte, V.; Ha, Y.; Mastroilli, P.; et al. Pt(II)-Decorated Covalent Organic Framework for Photocatalytic Difluoroalkylation and Oxidative Cyclization Reactions. *ACS Appl. Mater. Interfaces* **2021**, *13*, 6349–6358. [[CrossRef](#)]
49. Li, Y.; Yang, L.; He, H.; Sun, L.; Wang, H.; Fang, X.; Zhao, Y.; Zheng, D.; Qi, Y.; Li, Z.; et al. In Situ Photodeposition of Platinum Clusters on a Covalent Organic Framework for Photocatalytic Hydrogen Production. *Nat. Commun.* **2022**, *13*, 1355. [[CrossRef](#)]
50. Bika, P.; Ioannidis, N.; Gatou, M.A.; Sanakis, Y.; Dallas, P. Copper Coordination and the Induced Morphological Changes in Covalent Organic Frameworks. *Langmuir* **2022**, *38*, 3082–3089. [[CrossRef](#)]
51. Bratsos, I.; Tampaxis, C.; Spanopoulos, I.; Demetri, N.; Charalambopoulou, G.; Vourloumis, D.; Steriotis, T.A.; Trikalitis, P.N. Heterometallic In(III)-Pd(II) Porous Metal-Organic Framework with Square-Octahedron Topology Displaying High CO₂ Uptake and Selectivity toward CH₄ and N₂. *Inorg. Chem.* **2018**, *57*, 7244–7251. [[CrossRef](#)] [[PubMed](#)]
52. Zeng, Y.; Zou, R.; Zhao, Y. Covalent Organic Frameworks for CO₂ Capture. *Adv. Mater.* **2016**, *28*, 2855–2873. [[CrossRef](#)] [[PubMed](#)]
53. Dang, Q.Q.; Liu, C.Y.; Wang, X.M.; Zhang, X.M. Novel Covalent Triazine Framework for High-Performance CO₂ Capture and Alkyne Carboxylation Reaction. *ACS Appl. Mater. Interfaces* **2018**, *10*, 27972–27978. [[CrossRef](#)] [[PubMed](#)]
54. Zhang, M.; Zheng, R.; Ma, Y.; Chen, R.; Sun, X.; Sun, X. N-Rich Covalent Organic Frameworks with Different Pore Size for High-Pressure CO₂ Adsorption. *Microporous Mesoporous Mater.* **2019**, *285*, 70–79. [[CrossRef](#)]
55. Hug, S.; Stegbauer, L.; Oh, H.; Hirscher, M.; Lotsch, B.V. Nitrogen-Rich Covalent Triazine Frameworks as High-Performance Platforms for Selective Carbon Capture and Storage. *Chem. Mater.* **2015**, *27*, 8001–8010. [[CrossRef](#)]
56. Shiraishi, Y.; Kanazawa, S.; Kofuji, Y.; Sakamoto, H.; Ichikawa, S.; Tanaka, S.; Hirai, T. Sunlight-Driven Hydrogen Peroxide Production from Water and Molecular Oxygen by Metal-Free Photocatalysts. *Angew. Chem.-Int. Ed.* **2014**, *53*, 13454–13459. [[CrossRef](#)]
57. Shiraishi, Y.; Kanazawa, S.; Sugano, Y.; Tsukamoto, D.; Sakamoto, H.; Ichikawa, S.; Hirai, T. Highly Selective Production of Hydrogen Peroxide on Graphitic Carbon Nitride (g-C₃N₄) Photocatalyst Activated by Visible Light. *ACS Catal.* **2014**, *4*, 774–780. [[CrossRef](#)]
58. Zhu, B.; Zhang, L.; Xu, D.; Cheng, B.; Yu, J. Adsorption Investigation of CO₂ on G-C₃N₄ Surface by DFT Calculation. *J. CO₂ Util.* **2017**, *21*, 327–335. [[CrossRef](#)]
59. Giannakopoulou, T.; Papailias, I.; Todorova, N.; Boukos, N.; Liu, Y.; Yu, J.; Trapalis, C. Tailoring the Energy Band Gap and Edges' Potentials of g-C₃N₄/TiO₂ composite Photocatalysts for NO_xremoval. *Chem. Eng. J.* **2017**, *310*, 571–580. [[CrossRef](#)]

Disclaimer/Publisher's Note: The statements, opinions and data contained in all publications are solely those of the individual author(s) and contributor(s) and not of MDPI and/or the editor(s). MDPI and/or the editor(s) disclaim responsibility for any injury to people or property resulting from any ideas, methods, instructions or products referred to in the content.